RSC Advances

PAPER

View Article Online
View Journal | View Issue

Cite this: *RSC Adv.*, 2026, **16**, 19457

$Li_2CaP_2O_7$ pyrophosphate ceramics with dual functionality: high-performance NTC thermistor behavior and giant dielectric permittivity

O. Madkhali *[ab]

Inorganic pyrophosphate-based materials are widely recognized for their diverse functional properties, positioning them as strong contenders for a range of advanced technological applications. In this work, the compound $Li_2CaP_2O_7$ was synthesized and examined using a cost-efficient solid-state reaction route. Comprehensive structural and microstructural investigations were carried out to confirm phase purity and assess morphological features. Electrical studies performed between 373 and 673 K revealed semiconducting behavior governed by thermally activated hopping, characterized by a thermistor constant $\beta = 5554$ K, an activation energy $E_a = 0.49$ eV (± 0.01), and high temperature sensitivity (-4.0 to $-1\%/K^{-1}$), together with an excellent stability factor (SF = 3.02), underscoring its suitability for high-temperature sensing applications. Analysis of the Nyquist plots using an appropriate equivalent-circuit model allowed the separation of grain and grain-boundary effects. Notably, $Li_2CaP_2O_7$ exhibited an extremely large dielectric permittivity, on the order of 10^7 at low frequencies, along with low dielectric losses at higher frequencies. These features point to strong interfacial polarization consistent with the Maxwell–Wagner framework, and the material displays thermally activated, non-Debye-type relaxation dynamics. The interplay between charge transport and polarization mechanisms gives rise to the remarkable coexistence of NTC behavior and giant dielectric response. Altogether, these attributes establish $Li_2CaP_2O_7$ as a highly promising multifunctional material for integrated high-temperature sensing–capacitor devices and other advanced electronic systems.

Received 6th January 2026
Accepted 4th March 2026

DOI: 10.1039/d6ra00134c

rsc.li/rsc-advances

1. Introduction

The accelerated progress in modern technology and the increasing need for multifunctional electronic components have intensified the search for materials exhibiting extremely high dielectric constants (GDC). Such materials are essential for a wide range of industrial applications, including capacitors, data-storage systems, high-energy storage units, dynamic random-access memory, and various types of sensors. In this context, multifunctional ceramic compounds have gained considerable attention, as they offer promising properties for emerging electronic, sensing, and energy-storage technologies.[1,2] In this regard, phosphate-based compounds stand out for their structural versatility and wide applicability in biomedicine, gas detection, optoelectronics, and energy devices.[3–5] Among them, phosphate oxides exhibiting a negative temperature coefficient (NTC) of resistivity are particularly appealing, as their sharp decrease in resistance with temperature enables accurate and reliable thermistor performance.[5–7] Their high sensitivity, fast thermal response, low fabrication cost, and easy integration make them suitable for environmental monitoring, electronic temperature control, battery protection systems, and automotive safety.[5,8,9] A subclass of these compounds, pyrophosphate ceramics with the general formula $A_xMP_2O_7$ (A = alkali or alkaline-earth metal; M = divalent cation), is especially promising because their crystal frameworks favor ionic mobility and polarization processes,[10–16] allowing them to combine high dielectric permittivity with stable NTC behavior. Such characteristics are crucial for devices requiring both efficient charge-storage capability and dependable thermal sensing. Recent studies have highlighted this dual functionality for instance, $Li_2CoP_2O_7$ has shown exceptionally high low-frequency permittivity ($\sim 2 \times 10^8$ at 673 K),[10] while $TlFeP_2O_7$ exhibits pronounced NTC characteristics reinforcing the relevance of phosphate frameworks for multifunctional applications.[5] In these systems, electrical conduction commonly occurs *via* thermally activated hopping between mixed-valence phosphate units, generating polarons whose dynamics are strongly influenced by lattice distortions, vacancies, and electron–phonon interactions. Complex impedance spectroscopy (CIS) provides a powerful means to probe these processes,[17,18] enabling the separation of grain, grain-boundary, and electrode contributions to the overall response.

[a]*Nanotechnology Research Unit, Jazan University, P. O. Box. 114, Jazan 45142, Kingdom of Saudi Arabia. E-mail: osamam@jazanu.edu.sa*

[b]*Department of Physical Sciences, Physics Division, College of Science, Jazan University, P. O. Box. 114, Jazan 45142, Kingdom of Saudi Arabia*

Phosphates incorporating alkaline-earth cations, especially Ca^{2+}, provide a structurally stable and electronically simple framework that allows a more direct investigation of intrinsic hopping conduction and interfacial polarization phenomena. In contrast to transition-metal-based systems, the closed-shell configuration of Ca^{2+} reduces extrinsic electronic effects, facilitating a clearer analysis of charge transport mechanisms. For example, $NaCaP_3O_9$ (ref. 19) demonstrates thermally activated electrical conductivity along with a pronounced dielectric response arising from both grain and grain-boundary contributions. Its thermistor constant ($\beta = 3597$ K) and relatively low stability factor (SF = 1.5) reflect substantial temperature sensitivity while maintaining stable electrical behavior. These results emphasize the key role of Ca^{2+} in maintaining the structural integrity of the phosphate lattice while promoting favorable conduction and polarization properties. Consequently, Ca-containing pyrophosphates offer an excellent platform for exploring the interplay between electrical transport and dielectric phenomena in multifunctional ceramic materials.

Negative temperature coefficient (NTC) thermistors and high-permittivity dielectric materials have traditionally been developed as distinct functional categories. Materials designed for NTC applications are generally tailored to provide precise resistive responses to temperature variations, whereas high-k dielectrics are mainly optimized for energy storage and capacitive performance, with little emphasis on their thermal sensing capability. The simultaneous realization of both properties within a single inorganic phase is therefore relatively rare. From an application standpoint, however, combining pronounced temperature-dependent conductivity with a strong dielectric response in one material is highly advantageous, particularly for compact devices intended to operate in demanding or high-temperature environments. Such multifunctionality can only be achieved when electrical transport processes and polarization phenomena are intrinsically interconnected rather than occurring independently. In this regard, inorganic pyrophosphate structures represent an attractive platform because of their chemical robustness, adaptable conduction pathways, and significant interfacial polarization effects associated with microstructural features such as grains and grain boundaries. Investigating these coupled behaviors is thus of considerable scientific and practical relevance.

Building upon these insights, the present work offers a comprehensive investigation of $Li_2CaP_2O_7$, synthesized through a conventional solid-state method and sintered at 800 °C, to elucidate its structural, microstructural, dielectric, and electrical characteristics over wide temperature (373–673 K) and frequency (0.1–7 × 10^6 Hz) ranges. The compound demonstrates clear NTC thermistor behavior ($\beta = 5554$ K, $-4\%/K \leq \alpha \leq -1\%/K$, $E_a = 0.49$ eV, SF = 3.02), confirming its suitability for temperature-sensing applications, while its dielectric response reveals a giant low-frequency permittivity ($\varepsilon' \approx 10^7$ at 673 K) linked to effective interfacial polarization and thermally activated charge transport. At higher frequencies, the material maintains stable dielectric behavior with moderate energy losses. Collectively, these results position $Li_2CaP_2O_7$ as a promising dual-functional ceramic with strong potential for integrated sensing technologies, energy-storage components, and frequency-dependent dielectric devices.

2. Experimental methodology

2.1. Sample preparation

The $Li_2CaP_2O_7$ compound was prepared through a conventional solid-state reaction route. As outlined in Fig. 1, the synthesis followed several sequential steps to obtain a homogeneous final product. Accurately measured amounts of high-purity starting materials Li_2CO_3, $CaCO_3$, and $NH_4H_2PO_4$ were weighed in their stoichiometric ratios (0.64844 g, 0.87833 g, and 2.0189 g, respectively) and thoroughly ground together to ensure uniform mixing prior to heat treatment.

The balanced equation for the synthesis of this material, along with the physical states of each component, is presented below:

$$2\,NH_4H_2PO_4 + Li_2CO_3 + CaCO_3 = Li_2CaP_2O_7 + 3H_2O + 2\,CO_2 + 2\,NH_3 \quad (1)$$

The resulting powder was finely reground in an agate mortar for 2 hours to ensure complete homogeneity. The mixture was then pressed into 13 mm diameter pellets and preheated on a hot plate, followed by thermal treatment at 380 °C for 10 hours. During this stage, the sample mass was periodically checked until stabilization, corresponding to the release of NH_3, CO_2, and H_2O. The preheated material was then reground for 1 hour and pressed again into 8 mm pellets. These compacts were finally sintered at 800 °C for 4 hours to achieve a well-densified ceramic phase. The relative density of the $Li_2CaP_2O_7$ pellet was evaluated using a geometrical approach, considering its measured mass and physical dimensions. The pellet, having a diameter of 8 mm and a thickness of 1 mm, corresponds to a volume of approximately 0.0503 cm^3. With a measured mass of around 0.218 g, the experimental density was calculated using the expression $\rho_{exp} = m/V$,[20] resulting in a value of approximately 4.34 g cm^{-3}.

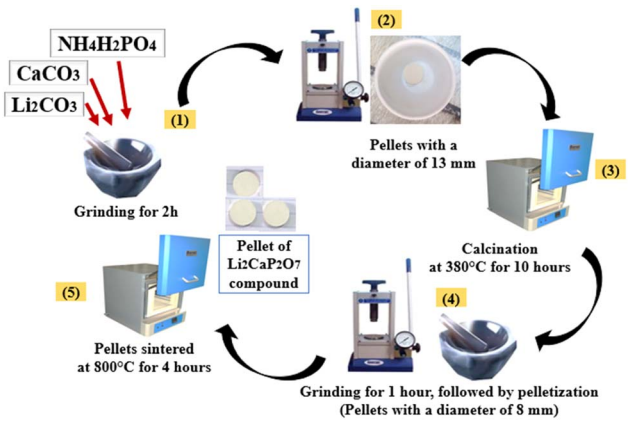

Fig. 1 Synthesis procedure of the $Li_2CaP_2O_7$ compound through the solid-state route.

2.2. Sample characterizations

The phase composition of the annealed sample was analyzed at room temperature using a Bruker D8 diffractometer with Cu Kα radiation (λ = 1.5406 Å) over a 2θ range of 10° to 70°. Morphological characterization was performed using a Merlin Scanning Electron Microscope (SEM), equipped with an energy-dispersive X-ray spectrometer (EDX).

Electrical and dielectric measurements were conducted using a Solartron 1260 impedance analyzer over a wide frequency range (0.1 Hz to 7 MHz) and a temperature interval of 373–673 K. These measurements were designed to probe the respective contributions of grains and grain boundaries to the electrical behavior of the $Li_2CaP_2O_7$ ceramics. The samples, prepared as discs of 8 mm in diameter and approximately 1 mm in thickness, were coated on both sides with a thin layer of silver to provide stable and low-resistance electrical contacts. The coated pellets were positioned between copper or platinum electrodes inside a temperature-regulated chamber equipped with a closed-loop control system, ensuring a temperature resolution of 0.1 K and stability better than 0.5 K. All experiments were performed under ambient pressure using an applied AC signal of 1 V, guaranteeing reliable data across the entire temperature and frequency domains. This methodology enabled a comprehensive assessment of the NTCR behavior and dielectric response of the synthesized $Li_2CaP_2O_7$ pyrophosphate.

3. Results and discussion

3.1. Structural and microstructural analysis

X-ray diffraction (XRD) is a key technique for probing the structural properties of ceramic materials. Fig. 2 displays the refined diffraction pattern of the lithium calcium pyrophosphate powder, recorded at room temperature over the 2θ range of 10°–70°. Structural refinement of the experimental pattern was performed using the FullProf suite[21] to obtain accurate crystallographic information. In the plot, the red symbols correspond to the measured intensities, while the black continuous curve represents the calculated profile. The blue vertical ticks mark the expected Bragg peak positions of the $Li_2CaP_2O_7$ phase. The green line shows the difference between the calculated and observed data; its nearly flat appearance indicates an excellent agreement and confirms the reliability of the refinement. Table 1 compiles the refined structural parameters and experimental conditions for $Li_2CaP_2O_7$. The refined unit cell parameters closely match those reported for analogous triclinic ($P\bar{1}$) $Ca_2P_2O_7$-type compounds, underscoring the structural consistency and stability of the synthesized material.[22–24] The *R*-factors (R_p = 31.9%, R_{wp} = 33.1%, R_{exp} = 14.55%) and the χ^2 value of 5.18 serve as indicators of the quality of the Rietveld profile refinement. R_p and R_{wp} reflect the differences between the measured and calculated diffraction patterns, with smaller values indicating closer agreement. R_{exp} corresponds to the expected *R*-factor derived from counting statistics, while χ^2 (calculated as R_{wp}^2/R_{exp}^2) assesses how the weighted fit compares to this expectation.

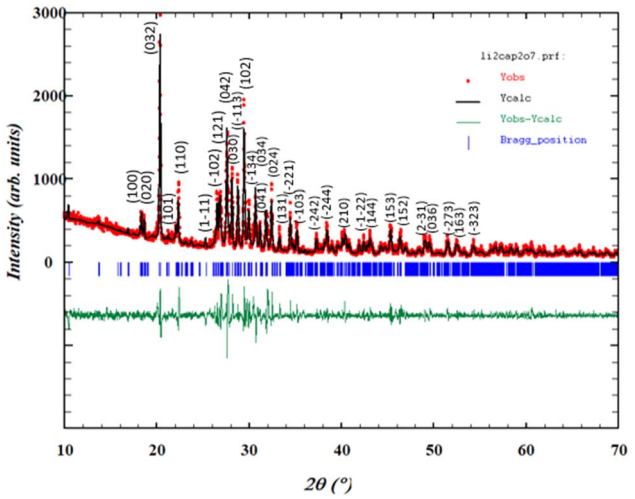

Fig. 2 XRD Rietveld refined pattern of $Li_2CaP_2O_7$ pyrophosphate calcined at 800 °C.

Table 1 Refined structural parameters of $Li_2CaP_2O_7$ compound at room temperature

Formula	$Li_2CaP_2O_7$
Crystalline system	Triclinic
Space group	$P\bar{1}$
Lattice parameters	
a (Å)	5.289
b (Å)	14.276
c (Å)	12.454
α	42.959
β	110.734
γ	113.331
Refinement parameters	
R_p (%)/R_{wp} (%)/R_{exp} (%)	31.9/33.1/14.55
χ^2	5.18

Fig. 3 displays the energy-dispersive X-ray (EDS) spectrum of the $Li_2CaP_2O_7$ compound. The identified peaks associated with Ca, P, and O confirm the formation of the intended phase. As expected, no lithium signal is observed due to the detection limits of the instrument. The carbon peak arises from the carbon tape used as the sample holder. The absence of any additional elements further verifies the successful synthesis of pure $Li_2CaP_2O_7$. Simultaneously, the inset table in Fig. 3 provides a quantitative evaluation of the elemental composition obtained from the EDX spectrum in terms of atomic percentages. A comparison between the experimental data and the calculated stoichiometric values demonstrates the reliability of the synthesis procedure and confirms the compositional consistency of the prepared material.

The surface morphology of the material was investigated using scanning electron microscopy (SEM) to gain deeper insight into its microstructural characteristics. The Fig. 4 shows SEM images of $Li_2CaP_2O_7$ annealed at 800 °C, captured at a 5 μm scale under high magnification. The micrographs reveal a dense structure made up of well-defined grains with minimal

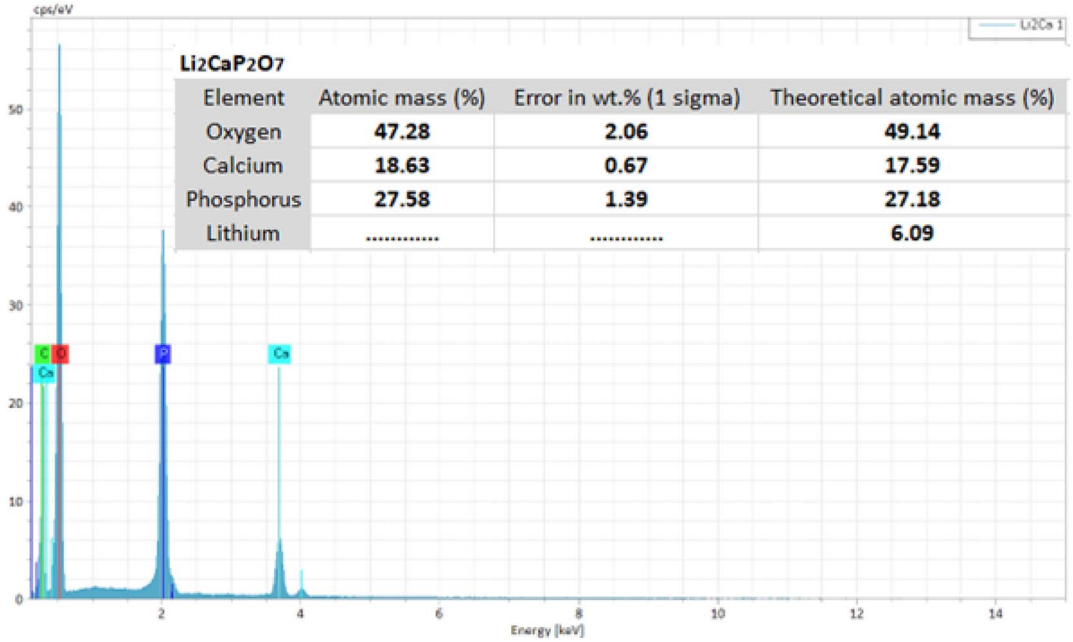

Fig. 3 Elemental analysis by EDX.

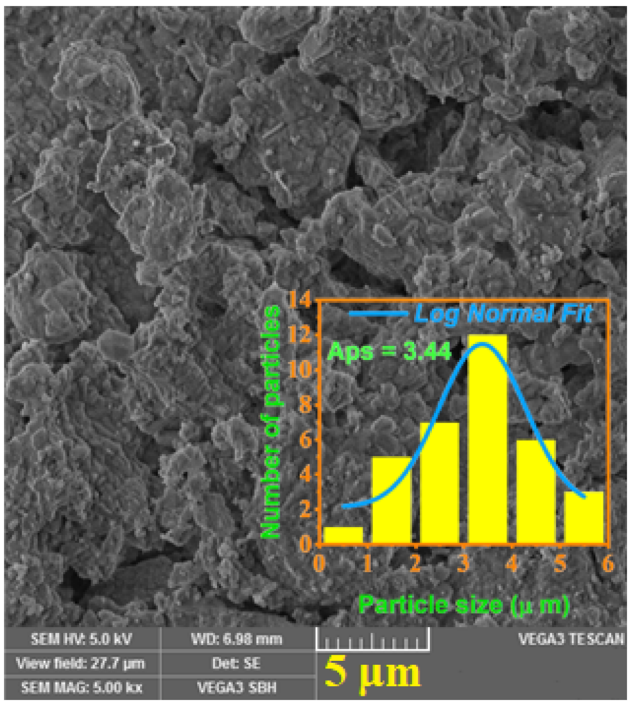

Fig. 4 SEM image and particle size distribution.

pore distribution, indicating efficient densification. This low porosity suggests effective sintering during the thermal treatment, which is beneficial for both the mechanical robustness and the electrical performance of the $Li_2CaP_2O_7$ sample. Fig. 4 shows the grain size distribution histogram obtained using a fitting procedure. The image analysis reveals an average grain size of about 3.44 μm.

3.2. Electrical properties

3.2.1. Negative temperature coefficient (NTC) characteristics. Fig. 5 depicts the evolution of the real part of the impedance, $Z'(\omega)$, for $Li_2CaP_2O_7$ over the temperature interval 373–673 K. A systematic decrease in Z' with increasing temperature is evident across the entire frequency domain, reflecting the thermally activated nature of charge transport and confirming the negative temperature coefficient (NTC) behavior of the ceramic.[25] At low frequencies, Z' exhibits a high plateau, mainly governed by grain-boundary resistances and interfacial

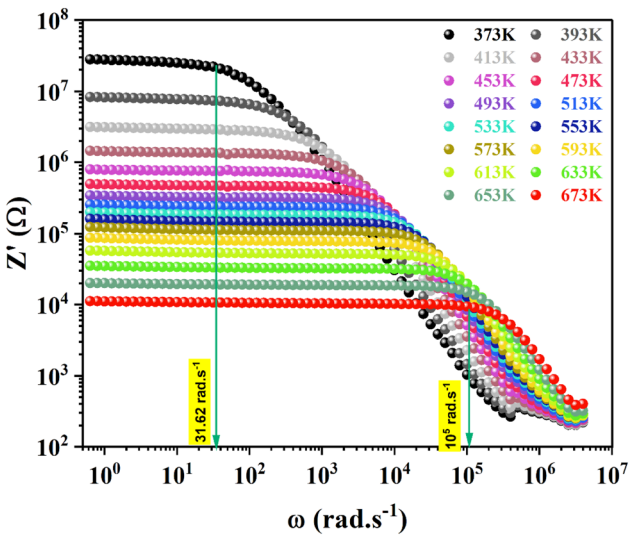

Fig. 5 Plots of the real component of the complex impedance of $Li_2CaP_2O_7$ pyrophosphate as a function of angular frequency over the temperature range 373–673 K.

polarization effects. As the frequency rises, Z' gradually drops, marking the onset of relaxation phenomena and the reduced influence of interfacial regions. This dispersion shifts toward higher frequencies at elevated temperatures, indicating accelerated charge-carrier dynamics. At the high-frequency end, Z' reaches a low, nearly constant value associated with the intrinsic response of the grains. The characteristic transitions observed around 31.62 rad s^{-1} and 10^5 rad s^{-1} highlight the changeover from interfacial contributions at low frequencies to grain-dominated conduction at higher frequencies, underscoring the strong thermal activation of mobile carriers and the consequent improvement in electrical conductivity.[26]

Building upon the behavior revealed by $Z'(\omega)$, Fig. 6 presents the complementary response of the imaginary part of the impedance, $-Z''(\omega)$, over the same temperature range. Consistent with the trend observed in the real component, $-Z''$ curves display broad relaxation peaks that migrate to higher frequencies as the temperature increases, further confirming the thermally driven nature of the relaxation process.[26,27] The progressive reduction in peak height with heating reflects a decrease in overall resistance, characteristic of semiconducting materials. Moreover, the asymmetric and broadened shape of the peaks signifies the presence of multiple relaxation times, pointing to a non-Debye type of relaxation.[26,28] Together, the Z' and $-Z''$ analyses offer a coherent picture of $Li_2CaP_2O_7$'s electrical behavior, highlighting its strong temperature dependence and reinforcing its potential as an efficient NTC thermistor material.[5,7,17]

The impedance analysis offers valuable information about the electrical behavior of a solid by revealing how its resistive and reactive components respond to changes in frequency and temperature.[7] In Fig. 7, the Nyquist plots recorded at different temperatures presented as $-Z''$ *versus* Z' show well-defined semicircular arcs. These arcs point to a dominant grain-boundary contribution, emphasizing the crucial role of both

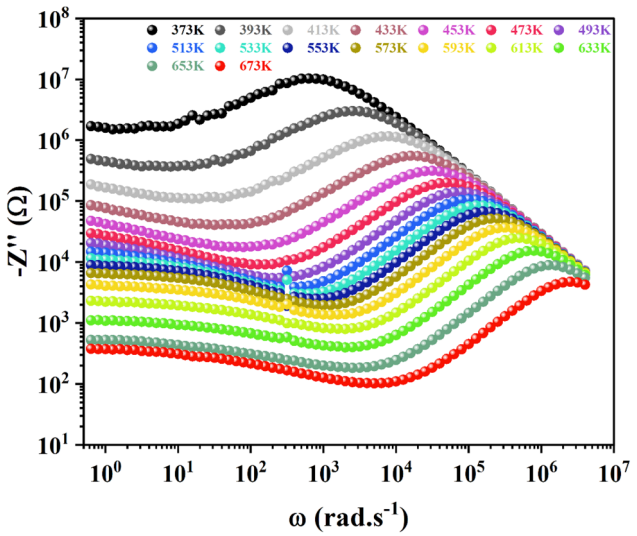

Fig. 6 Plots of the imaginary component of the complex impedance of $Li_2CaP_2O_7$ pyrophosphate as a function of angular frequency over the temperature range 373–673 K.

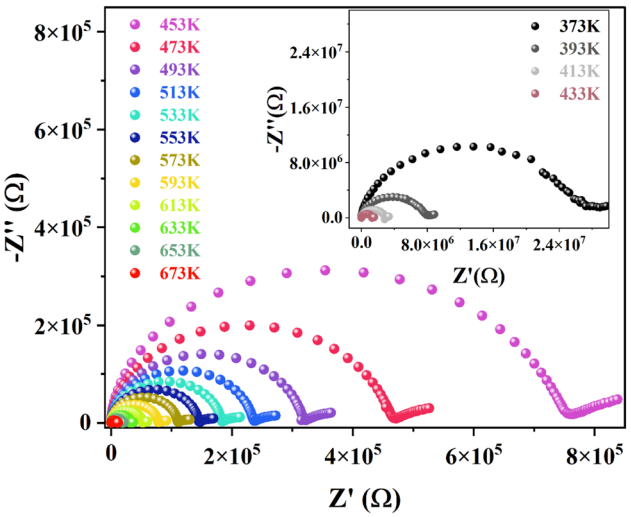

Fig. 7 Observed impedance complex plane plots of the $Li_2CaP_2O_7$ compound.

the resistive and capacitive elements associated with these boundaries in shaping the overall impedance response of $Li_2CaP_2O_7$. At low frequencies, an additional feature emerges that is linked to electrode polarization. This effect stems from charge build-up at the electrode–sample interface, a behavior often encountered in dielectric and semiconducting materials.[29] With increasing temperature, the diameter of the semicircles shrinks considerably, reflecting a conduction mechanism that becomes more efficient as thermal energy rises. Higher temperatures promote greater charge-carrier mobility, which in turn leads to a noticeable decrease in resistance.[30,31] Such a trend is characteristic of semiconductors and confirms the strong temperature dependence of their transport properties. The observed behavior is consistent with an Arrhenius-type process, in which charge carriers must surmount activation barriers to contribute to electrical conduction.

To accurately interpret the impedance data, an appropriate Equivalent Circuit Model (ECM) is selected. The choice of ECM is guided by the observed impedance characteristics and involves simulating the material's behavior with a combination of resistors, capacitors, and constant phase elements (CPEs).[32] The precise selection of an ECM is essential for quantifying key electrical parameters, such as resistance and capacitance. For $Li_2CaP_2O_7$, the impedance plane plots were analyzed to determine the best-fit equivalent circuit model. The optimal fit was achieved using an electrical circuit consisting of a parallel combination of a resistor (R), a capacitor (C), and a constant phase element (CPE_1), connected in series with an additional constant phase element (CPE_2). This configuration is depicted in the Fig. 8.

The CPE element is described by the expression:[33]

$$Z_{CPE_i} = \frac{1}{Q_i(j\omega)^{\alpha_i}} \quad (2)$$

Here, (j) represents the imaginary unit, (ω) denotes the angular frequency, and (α_i) is a constant with a value between 0 and 1.

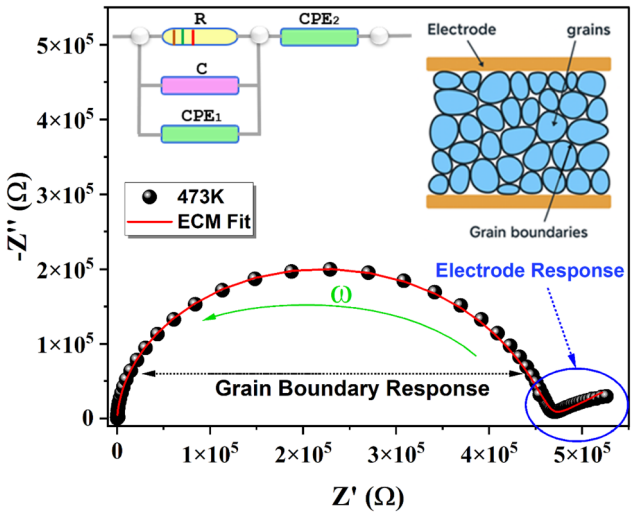

Fig. 8 Complex impedance plots at 473 K, together with the fitted equivalent circuit, are presented alongside a schematic illustrating grains and grain boundaries within the ceramic between the two electrodes.

The constant phase element (CPE) is used to describe the non-ideal capacitive response observed in our samples, which can result from microstructural factors such as grain boundaries, surface irregularities, or a spread in relaxation times. The CPE is defined by two parameters: Q, representing a pseudo-capacitance, and α, an exponent ($0 < \alpha \leq 1$) that quantifies the deviation from an ideal capacitor. In our measurements, α increases with temperature and approaches unity at higher temperatures, indicating that the material behaves more like an ideal capacitor as thermal activation improves ion mobility and reduces inhomogeneities. The key electrical parameters extracted from the analysis are summarized in Table .2. This table emphasizes three major conclusions derived from the data: (1). Temperature Dependence of Grain Boundary Resistance: the resistance of the grain boundaries decreases with increasing temperature, attributed to thermally activated charge carriers that enhance mobility. (2). Distinct capacitance ranges are observed: approximately 10^{-11} F for grains, 10^{-10} F for grain boundaries, and 10^{-5} F for the electrode contribution, reflecting the different electrical responses of these components. (3). Relaxation Mechanism: The parameters α_1 and α_2 consistently remain within the range of 0 to 1 across all temperatures, indicating that the relaxation mechanism in $Li_2CaP_2O_7$ follows a non-Debye-type behavior throughout the studied frequency and temperature range.[34]

3.2.2. Electrical resistance and activation energy. Fig. 9 presents the variation of electrical resistivity with temperature for the synthesized pyrophosphate over the range 373–673 K. The resistivity decreases exponentially as the temperature rises, a clear indication of the material's semiconducting character. This thermally activated behavior is consistent with the Steinhart–Hart relation,[32,33] further demonstrating that $Li_2CaP_2O_7$

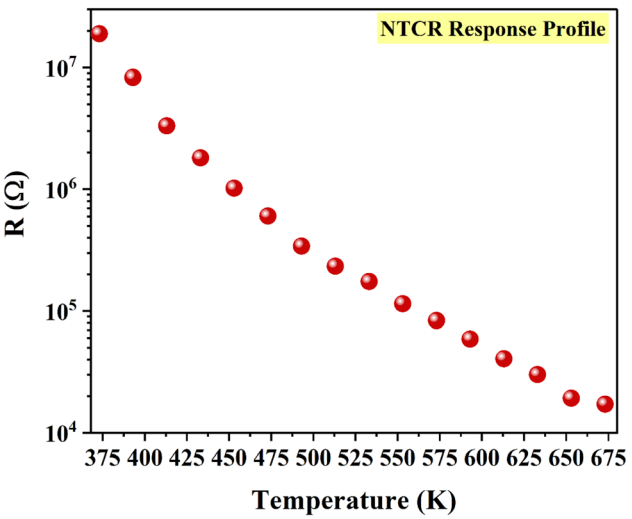

Fig. 9 Variation of resistance with temperature.

Table 2 The deduced electrical parameters, using the Z-View software

T (K)	R (10^5 Ω)	C (10^{-11} F)	Q_1 (10^{-10} F)	α_1	Q_2 (10^{-5} F)	α_2	χ^2
373	189.589	3.4866	6.6345	0.51409	0.061763	0.60113	0.0015
393	82.974	3.433	13.77	0.47884	0.17468	0.53112	0.0011
413	33.17474	3.435	21.79	0.46627	0.39684	0.47268	0.0008
433	18.10599	3.457	25.03	0.47343	0.77803	0.42886	0.0011
453	10.19424	3.452	16.03	0.53429	1.3316	0.39634	0.0007
473	6.03959	3.459	11.11	0.57265	1.8261	0.36129	0.0005
493	3.41978	3.452	59.07	0.63126	2.3533	0.33492	0.0004
513	2.33810	3.486	3.415	0.67441	2.8022	0.30916	0.0005
533	1.74389	3.496	2.097	0.70537	3.2018	0.28876	0.0004
553	1.14721	3.606	1.9	0.69912	3.7511	0.27052	0.0004
573	0.83561	3.731	2.528	0.65433	4.6173	0.25159	0.0004
593	0.58999	3.885	5.476	0.57689	6.5952	0.22762	0.0005
613	0.40610	3.912	2.966	0.62053	0.010911	0.19714	0.0003
633	0.30086	3.874	0.5126	0.77651	0.020028	0.1611	0.0002
653	0.19239	2.919	0.7736	0.99353	0.037715	0.12361	0.0001
673	0.17132	0.1051	11.02	0.99952	0.051913	0.096827	0.0005

possesses the characteristics required for efficient high-temperature thermistor applications.

The Fig. 10 depicts the relationship between ln(R) and the reciprocal of temperature ($1/K_BT$) for the studied compound. The resulting plot demonstrates a strong linear trend, indicating a consistent decrease in resistivity with rising temperature and confirming the material's excellent NTCR characteristics. Within the examined temperature range, the curve adheres to the Arrhenius equation, which describes the proportional relationship between electrical resistivity and temperature.[34]

$$R(T) = R_0 \exp\left(\frac{-E_a}{K_B T}\right) \quad (3)$$

In this expression, R_0 corresponds to the resistivity pre-exponential factor, K_B is Boltzmann's constant, and E_a denotes the activation energy. The trends observed in Fig. 10, together with the application of this relation, clearly demonstrate that the synthesized material follows an Arrhenius-type conduction mechanism. Such behavior confirms its strong suitability for thermistor applications. The consistency of its resistivity response across the studied temperature range highlights the compound's excellent potential for accurate temperature sensing, offering both high stability and notable sensitivity under varying thermal conditions.

Moreover, the extracted activation energy of E_a = 0.49 eV (±0.01) reinforces the favorable electrical characteristics of the material. When compared with related systems such as $Li_2SrP_2O_7$, which exhibits a higher activation energy of 1.03 eV in the range 519–628 K (ref. 14) the obtained value for $Li_2CaP_2O_7$ falls within a moderate and advantageous range. Activation energy plays a crucial role in conductivity by influencing the rate at which Li^+ ions rearrange between sites.[35] Additionally, the high crystallinity of $Li_2CaP_2O_7$ in its pyrophosphate structure further enhances the resilience and efficiency of the Li^+ ion transport mechanism, ensuring excellent ionic mobility.

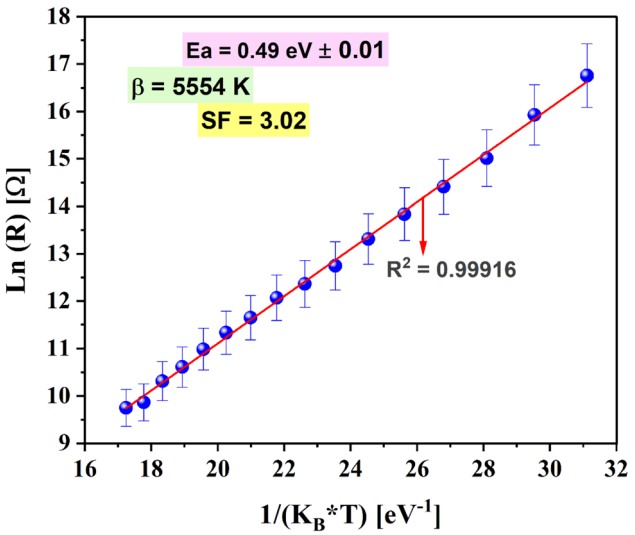

Fig. 10 Variation of ln(R) with $1/(K_B \cdot T)$ and the corresponding electrical parameters derived.

3.2.3. Sensitivity or thermistor constant (β). The β factor is the most crucial parameter for describing and evaluating any thermistor material or component. It represents the sensitivity constant of the thermistor material, serving as a quantitative measure of its response to temperature variations. According to the literature,[36–38] the β parameter is primarily used to validate the strong correlation between a material's resistivity and changes in temperature. For the pyrophosphate sample under study, the β value can be determined from the slope of the linear plot of ln(R) *versus* $1/(K_B \times T)$ (Fig. 10). This slope directly yields the activation energy, which is intrinsically linked to the sensitivity parameter. The sensitivity constant β and the activation energy are further connected through the following relationship:[39]

$$\beta = \frac{E_a}{K_B} \quad (4)$$

The deduced sensitivity constant (β) is 5554 K. The calculated sensitivity factor is presented in Table .3 and compared with that of other studied compounds.

3.2.4. Temperature coefficient (α). The material characteristic, alpha (α), represents the percentage change in resistance per Kelvin (% K),[39,45] also known as the temperature coefficient or sensitivity index. This is a fundamental concept in thermistor calculations, as the resistance of an NTC thermistor depends on temperature. Fig. 11 illustrates the variation of the temperature coefficient (α) with temperature. The temperature coefficient was determined from the resistance temperature (R–T) characteristics. Since the resistance of NTC thermistors varies non-linearly, the α value is also nonlinear for a given thermistor material,[46–48] which explains the sensor's rapid thermal response. Consequently, the temperature dependence of the parameter α is related to the sensitivity factor β through the following equation:[49]

$$\alpha(T) = -\frac{\beta}{T^2} \times 100 \quad (5)$$

For an efficient thermistor material with promising performance, the sensitivity index α is typically expected to fall within the range of −1 to −9%.[39] This aligns well with our findings, where α varies between −1% and −4.5%.

3.2.5. Stability factor (SF). A stability test was conducted using the well-established stability factor formula,[50,51] a common method for assessing the reliability and performance

Table 3 NTCR compounds with diverse sensitivity (β) values for sensor devices thermistor application

Compounds	Sensitivity (β)	References
$Li_2CaP_2O_7$	5554 K	This work
$NaCaP_3O_9$	3597 K	19
ZnO	8079.93 K	36
LaCrNiMnO	2350 K	40
$Cu_{0.2}Ni_{0.5}ZnMn_{1.3}O_4$	3356 K	41
Y_2O_3–Mn_2O_3–Cr_2O_3	3600 K	42
$Mn_{1.56}Co_{0.96}Ni_{0.48}O_4$	2972–3035 K	43
Ag_2S–Ag	1250–2684 K	44

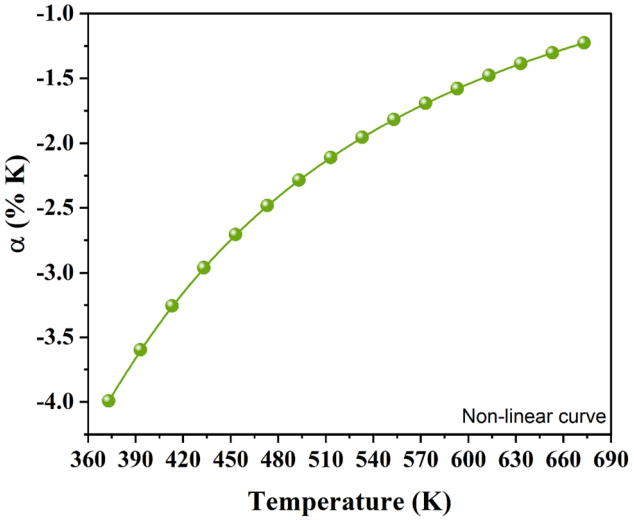

Fig. 11 Variation of sensitivity index (α) with temperature.

of materials under varying conditions. The stability factor (SF) is mathematically expressed as the logarithmic ratio of the maximum resistivity (R_{max}) to the minimum resistivity (R_{min}) within a specific temperature range:

$$SF = \log\left(\frac{R_{max}}{R_{min}}\right) \quad (6)$$

This parameter serves as a valuable indicator of the uniformity and stability of resistivity data points under thermal variations, reflecting the material's ability to maintain consistent performance across a range of operating temperatures. For the studied system, the calculated stability factor is SF = 3.02 (Fig. 10), signifying a notable degree of thermal stability. Smaller resistivity fluctuations, as indicated by this value, are a marker of the material's reliability and robustness for practical applications. Compared to previously reported values for some materials in the literature, this encouraging result underscores the strength and durability of the investigated sample. The relatively high stability factor highlights the material's inherent structural and electronic uniformity, making it a strong contender for sensor applications.[43,51]

3.3. Dielectric response: frequency dependence of the permittivity (ε)

The complex impedance (Z) of the sample was then converted into the complex permittivity (ε) using the relation given below:[52]

$$\varepsilon^* = \varepsilon' - j\varepsilon'' = \frac{1}{j\omega C_0 Z^*} \quad (7)$$

Here, (ε'), (ε''), and (ω) retain their standard definitions, while ($C_0 = \varepsilon_0 A/d$) represents the capacitance of the empty cell, where 'A' denotes the sample's surface area, and 'd' is its thickness.

Fig. 12(a) displays the frequency- and temperature-dependent behavior of the real part of the dielectric permittivity (ε') for $Li_2CaP_2O_7$ in the 373–673 K temperature interval. At

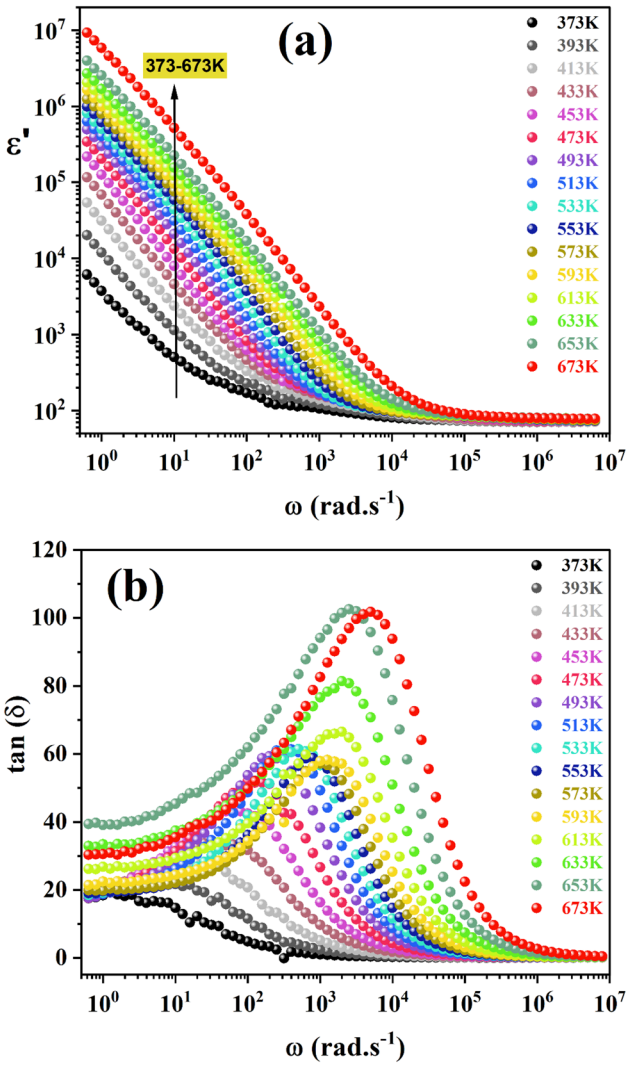

Fig. 12 (a). Frequency-dependent of real part of dielectric constants (ε'). (b). Variation of the dielectric loss factor with frequency at different temperatures.

low frequencies, ε' reaches very high values (around 10^7 at 673 K) which are compared to those reported for other members of the $Li_2XP_2O_7$ family (see Table .4), after which it decreases sharply with increasing frequency and eventually stabilizes at a much lower, nearly constant value in the high-frequency region for all temperatures. Such behavior is characteristic of Maxwell–Wagner interfacial polarization,[53,54] where charges accumulate at grain boundaries or interfaces, forming high-

Table 4 Comparative summary of the dielectric properties at height temperature of $Li_2XP_2O_7$ family materials reported in the literature

Compounds	Dielectric constant (ε') at high temperature	Temperature (K)	References
$Li_2CaP_2O_7$	10^7 (0.1 Hz)	673	This work
$Li_2CoP_2O_7$	2×10^8 (0.1 Hz)	673	10
$Li_2CuP_2O_7$	10^3 (209 Hz)	710	53
$Li_2BaP_2O_7$	140 (200 Hz)	724	16

resistance barriers at the electrodes and leading to an increased dielectric response at lower frequencies. The relaxation behavior is also governed by dipolar polarization, arising from dipole rotation or deformation associated with ionic and electronic displacement mechanisms.[55,56] With increasing frequency, these dipoles fail to keep pace with the rapidly alternating field, leading to the observed rapid decline in ε'. At sufficiently high frequencies, charge carriers and vacancies are unable to follow the applied field, causing the permittivity to become frequency-independent and lower due to the diminishing contribution of orientational polarization and the predominance of interfacial effects. The temperature evolution of the curves in Fig. 12(a) shows a clear increase in ε' with rising temperature, confirming that dipole alignment is thermally activated. At lower temperatures, insufficient thermal energy limits dipole mobility, resulting in smaller permittivity values. As the temperature increases, the added thermal energy enhances dipole motion and reorientation, which in turn boosts the dielectric response and yields higher ε' values at elevated temperatures.

The loss factor represents the ratio between the energy dissipated (ε'') and the energy stored (ε') in the material.[57] It was determined using the following expression:

$$\tan\ \delta = \frac{\varepsilon''}{\varepsilon'} \tag{8}$$

Fig. 12(b) presents the frequency-dependent dielectric loss ($\tan\delta$) of the $Li_2CaP_2O_7$ pyrophosphate, showing a clear decrease in loss with increasing frequency. In this compound, structural imperfections, and grain-boundary regions act as potential barriers that limit the mobility of charge carriers, in accordance with Koop's theory.[58,59] At low frequencies, these carriers accumulate at the grain boundaries, producing pronounced space-charge polarization. This accumulation demands additional energy for carriers to overcome the barrier, which explains the relatively high $\tan\delta$ values observed in the low-frequency region for $Li_2CaP_2O_7$. The dielectric loss spectrum of $Li_2CaP_2O_7$ also reveals distinct relaxation peaks, which are associated with space-charge and dipolar polarization processes inherent to its pyrophosphate structure. With increasing temperature, a clear shift in the relaxation peak is observed. At 373 K, the peak is located at approximately 3.96 rad s^{-1} with a maximum value close to 17. When the temperature reaches 673 K, the peak moves to about 4.9×10^3 rad s^{-1} and its intensity increases to nearly 101. This progressive shift toward higher frequencies, accompanied by an enhancement of the loss magnitude, confirms the thermally activated behavior of charge carriers and dipolar relaxation processes in the material. This shift reflects the enhanced mobility within the Li–O and Ca–O sublattices, which facilitates faster polarization processes at elevated temperatures. At higher frequencies, the loss factor significantly decreases because the charge carriers in $Li_2CaP_2O_7$ are unable to keep up with the rapidly oscillating electric field, resulting in reduced conduction losses. Additionally, $\tan\delta$ increases with temperature, indicating that thermal activation promotes carrier hopping and dipole reorientation within the phosphate network. A noteworthy feature

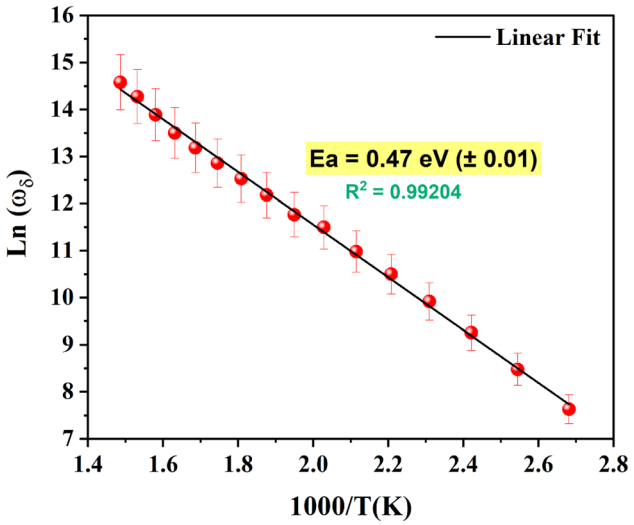

Fig. 13 The plot of $\ln(\omega_\delta)$ as a function of the inverse temperature.

of $Li_2CaP_2O_7$ is its relatively low dielectric loss in the high-frequency region, which is an essential requirement for energy-storage and battery-related applications.[60,61] The combination of thermally activated polarization, reduced loss at high frequencies, and stable dielectric behavior highlights $Li_2CaP_2O_7$ as a promising material for advanced electrochemical and solid-state device applications.

Fig. 13 presents the $\ln(\omega_\delta)$ *versus* $1000/T$ plot, where ω_δ denotes the angular frequency associated with grain-boundary relaxation. The temperature dependence of ω_δ adheres to the Arrhenius relation, expressed as follows:

$$\omega_\delta(T) = \omega_0 \exp\left(\frac{-E_a}{K_B T}\right) \tag{9}$$

Here, E_a represents the activation energy. From the slope of the linear fit in Fig. 13, E_a was determined to be 0.47 eV (±0.01). This value, which closely matches the activation energy derived from impedance analysis, demonstrates a strong link between

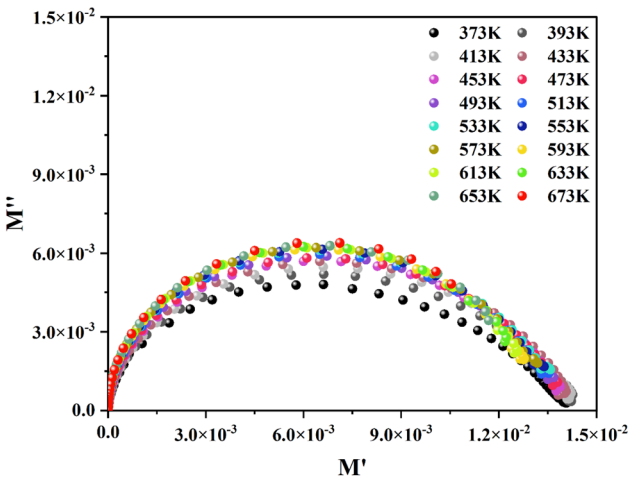

Fig. 14 Complex diagrams of electric modulus, at various temperatures.

the relaxation behavior and the charge-transport mechanism in the $Li_2CaP_2O_7$ compound.[9,60]

A comprehensive investigation was carried out using the electric modulus approach ($M^* = 1/\varepsilon^*$) in order to more effectively differentiate intrinsic bulk relaxation from extrinsic interfacial effects. The analysis of the real (M') and imaginary (M'') components of the modulus reduces the influence of electrode polarization and enables a more accurate evaluation of the bulk dielectric response. Fig. 14 illustrates the M'' *versus* M' representations recorded between 373 and 673 K. The lack of a separate low-frequency semicircular feature in the modulus plane confirms that electrode-related polarization is not a dominant contribution within the studied temperature range.[6,9] Instead, the dielectric behavior at low frequencies is primarily controlled by grain-boundary effects, which are responsible for the interfacial polarization mechanism.

4. Conclusion

In this work, high-purity reagents ($CaCO_3$, $NH_4H_2PO_4$, and Li_2CO_3) were employed to produce $Li_2CaP_2O_7$ pyrophosphate electroceramic *via* a conventional solid-state reaction. After sintering at 800 °C for 4 h, the material attained a single-phase composition. X-ray diffraction (XRD) and EDX-SEM morphological analysis revealed that the compound crystallizes in a triclinic lattice, with space group $P\bar{1}$. Electrical characterization, carried out over the temperature range 373–673 K, utilized Nyquist plots whose response was successfully modeled using an equivalent circuit. The results yield a thermistor constant β of 5554 K, an activation energy $E_a \approx 0.49$ eV, and a high temperature sensitivity of −4.0 to −1% K^{-1}, along with a robust stability factor (SF ≈ 3.02). Remarkably, $Li_2CaP_2O_7$ exhibits a very high dielectric permittivity on the order of $\sim 10^7$ at low frequencies while maintaining low dielectric losses at elevated frequencies. Loss-tangent measurements further point to thermally-activated hopping as the dominant conduction mechanism. The close correspondence between the activation energies obtained from loss-tangent data and impedance spectroscopy strongly suggests that the same mobile charge carriers govern both dielectric relaxation and conduction processes. Overall, these results suggest that $Li_2CaP_2O_7$ may be considered a promising candidate for high-temperature sensing environments, including power-battery systems, exhaust-gas monitoring, and engine-control units. Its semiconducting nature and thermally activated conduction behavior are consistent with materials employed in NTC thermistors, energy-storage, and sensing technologies. However, the present study is confined to fundamental structural and electrical characterization. Consequently, such applications should be regarded as prospective, and additional investigations addressing long-term stability, reproducibility, and device-level validation are necessary to establish its practical applicability.

Conflicts of interest

The authors declare that they have no known financial interests or personal relationships that could have influenced the work presented in this paper.

Data availability

The authors confirm that the data used to support the findings of this study are included within the article and are available from the corresponding author upon reasonable request.

Acknowledgements

This article is derived from a research grant funded by the Research, Development, and Innovation Authority (RDIA) – Kingdom of Saudi Arabia – with grant number (12894-JAZZAN-2023-JZU-R-2-1-SE)

References

1 L. Meng, *et al.*, Photoluminescence and electrical properties of Ho3+-doped Bi4Ti3O12 multifunctional ceramics, *Ceram. Int.*, 2025, **51**(27), 53204–53214, DOI: 10.1016/j.ceramint.2025.09.071.
2 Y. Wang, Y. Chen and D. Zheng, Development of multifunctional electronic-ceramics with piezoelectric effect and varistor behavior, *Ceram. Int.*, 2022, **48**(18), 26818–26827, DOI: 10.1016/j.ceramint.2022.05.383.
3 X. Yuan, T. Wu, T. Lu and J. Ye, Comparison of physicochemical and biological properties of calcium phosphate cements incorporating different strontium-containing compounds, *Ceram. Int.*, 2025, **51**(29), 60094–60105, DOI: 10.1016/j.ceramint.2025.10.208.
4 N. Y. Aldaleeli, H. M. Abd El-Lateef, T. A. Hamdalla, A. A. Taha, A. M. Alsharari and M. M. Khalaf, The photocatalytic and sensing performance of newly fabricated double phosphate compounds CuNiPO4 and MnNiPO4 for possible use in sensing applications, *Ceram. Int.*, 2025, **51**(17), 23180–23192, DOI: 10.1016/j.ceramint.2025.03.007.
5 I. Garoui, *et al.*, Dielectric relaxation and electrothermal charge carrier transport *via* correlated barrier hopping in the solid electrolyte TlFeP2O7: Experimental and theoretical modeling, *Ceram. Int.*, 2025, **51**(19), 29510–29525, DOI: 10.1016/j.ceramint.2025.04.155.
6 M. Karray, I. Garoui, M. Akermi, R. Djebali, A. Oueslati and M. Gargouri, Implementing a solid-state synthesis route to tune the functional properties of NaCdP3O9 metaphosphate: optical characteristics, ionic conductivity, and dielectric behavior, *RSC Adv.*, 2025, **15**(36), 29703–29719, DOI: 10.1039/d5ra04138d.
7 M. Karray, I. Garoui, S. Nasri, S. Znaidia, A. Mahmoud and A. Oueslati, Cesium Iron (III) Pyrophosphate Prepared Using a Solid-State Process: Structure, Mössbauer Spectroscopy, and Relaxation Dynamics, *ChemistrySelect*, 2025, **10**(2), 1–10, DOI: 10.1002/slct.202404727.
8 L. Lukaviciute, *et al.*, Cationic substitution effects in phosphate-based bioceramics - A way towards superior bioproperties, *Ceram. Int.*, 2024, **50**(19), 34479–34509, DOI: 10.1016/j.ceramint.2024.06.398.
9 I. Garoui, S. Ben Yahya, N. A. Alghamdi, I. Chaabane, A. Oueslati and B. Louati, Investigation of electronic

parameters, carrier transport mechanisms *via* the correlated barrier hopping model, electrothermal NTCR effects, and polarization contributions to the dielectric response of Ni3(PO4)2 orthophosphates synthesized by the sintering process, *Mater. Adv.*, 2025, **6**, 9761, DOI: 10.1039/d5ma01096a.

10 S. Aydi, A. Djemli, O. A. Algethami, S. Znaidia, F. Sahnoune and A. Oueslati, Study on morphological, FTIR, optical band-gap and AC conductivity of Li2CoP2O7 for advanced applications, *RSC Adv.*, 2025, **15**(33), 27154–27166, DOI: 10.1039/d5ra04105h.

11 R. Achagar, *et al.*, A Green and Efficient Protocol for the Synthesis of Phenylhydrazone Derivatives Catalyzed by Nanostructured Diphosphate Na2CaP2O7 and Screening of Their Antibacterial Activity, *ChemistrySelect*, 2021, **6**(6), 1366–1371, DOI: 10.1002/slct.202004671.

12 R. Mendil, S. Nasri and A. Oueslati, Structural investigation, vibrational study, and Na-ion transport properties of NaGaP2O7 as sodium solid electrolyte, *Ionics*, 2025, **31**(3), 2501–2514, DOI: 10.1007/s11581-025-06087-6.

13 M. Karray, S. Nasri, R. Mendil, I. Kammoun, A. Mahmoud and A. Oueslati, Studies on Structural and Ionic Conductivity of Li2NiP2O7, *ECS J. Solid State Sci. Technol.*, 2023, **12**(11), 113011, DOI: 10.1149/2162-8777/ad0ab2.

14 O. Ajili, B. Louati and K. Guidara, Dielectric and ac ionic conductivity investigation of Li2SrP2O7, *Indian J. Phys.*, 2018, **92**(7), 875–881, DOI: 10.1007/s12648-018-1182-8.

15 D. Ozer, Z. Ertekin, K. Pekmez and N. Altuntas Oztas, Fuel effects on Li2CuP2O7 synthesized by solution combustion method for lithium-ion batteries, *Ceram. Int.*, 2019, **45**(4), 4626–4630, DOI: 10.1016/j.ceramint.2018.11.151.

16 M. Krichen, M. Megdiche, K. Guidara and M. Gargouri, AC conductivity and mechanism of conduction study of lithium barium pyrophosphate Li2BaP2O7 using impedance spectroscopy, *Ionics*, 2014, **21**(4), 935–948, DOI: 10.1007/s11581-014-1261-6.

17 Y. Moualhi, M. Javed and H. Rahmouni, Dual functional behavior of nickel ferrite spinel oxide: High-performance NTC thermistor with relaxor ferroelectric characteristics, *Sens. Actuators, A*, 2025, **396**, 117212, DOI: 10.1016/j.sna.2025.117212.

18 I. Ouni, Y. Moualhi and H. Rahmouni, Thermistor and capacitor parameter analysis through electrical and dielectric investigations of manganite systems for technological applications, *Sens. Actuators, A*, 2025, **384**, 116300, DOI: 10.1016/j.sna.2025.116300.

19 M. Karray, I. Garoui, S. Nasri, N. A. Alsobai, N. A. Alghamdi and A. Oueslati, Enhanced optical, electrical and charge transport properties of NaCaP3O9 ceramics for emerging advanced technologies, *Mater. Adv.*, 2026, **7**(3), 1658–1677, DOI: 10.1039/d5ma01363a.

20 S. Ben Yahya, I. Garoui, A. Oueslati and B. Louati, Structural, Optical, and Conduction Relaxation Properties of TlCrP2O7 Driven by Nonoverlapping Small Polaron Tunneling, *ACS Omega*, 2026, **11**(4), 6227–6240, DOI: 10.1021/acsomega.5c10392.

21 J. Rodriguez-Carvajal, Magnetic Structure Determination From Powder Diffraction Using The Program FullProf, *Appl. Crystallogr.*, 2001, DOI: 10.1142/9789812811325_0005.

22 W. Sauskojus, J. K. Wied, C. F. Litterscheid, M. Mangstl and J. Schmedt auf der Günne, Crystal Structure of γ-Ca2P2O7, *Z. fur Anorg. Allg. Chem.*, 2022, **648**(21), 1–7, DOI: 10.1002/zaac.202200196.

23 J. Huang, *et al.*, Na2CaP2O7:Cr3+ phosphor toward broadband emission, *Optik*, 2024, **311**, 171958, DOI: 10.1016/j.ijleo.2024.171958.

24 J. Bennazha, A. Boukhari and E. M. Holt, Synthesis and crystal structure of Na2CaP2O7, *Solid State Sci.*, 1999, **1**(6), 373–380, DOI: 10.1016/s1293-2558(00)80091-6.

25 A. Raju, A. V. Babu, S. Jagtap and B. P. Kumar, Studies on structural and electrical properties of NTC thermistors, *J. Mater. Sci.: Mater. Electron.*, 2025, **36**(25), 1572, DOI: 10.1007/s10854-025-15633-x.

26 S. Aydi, I. Garoui, S. Nasri, M. Akermi, R. Djebali and A. Oueslati, Engineering spinel ferrites *via* A-site cation Substitution: Structural, electrical, and optical properties for advanced applications, *Ceram. Int.*, 2025, **51**(26), 48861–48877, DOI: 10.1016/j.ceramint.2025.08.136.

27 M. Toumi, Ah. Dhahri, A. Benali, R. Dhahri, B. F. O. Costa and E. Dhahri, Multifunctional lead-free La0.67Ca0.2Ba0.13Fe0.97Cr0.03O3 perovskite nanoceramics: Comprehensive structural, electrical, dielectric and gas sensing analysis, *J. Alloys Compd.*, 2025, **1048**, 185035, DOI: 10.1016/j.jallcom.2025.185035.

28 S. Nasri, A. Jraba, I. Garoui, A. Oueslati and E. Elaloui, Potassium tin chloride (K2SnCl6) as a lead-free perovskite: anti-solvent synthesis, structural characterization, and charge transport properties, *RSC Adv.*, 2025, **15**(7), 5369–5380, DOI: 10.1039/d5ra00090d.

29 S. B. Yahya and B. Louati, Characterization of the structure and conduction behavior of overlapping polaron tunnel of dipotassium zinc orthogermanate, *J. Alloys Compd.*, 2021, **876**, 159972, DOI: 10.1016/j.jallcom.2021.159972.

30 I. Garoui, M. Mallek, F. N. Almutairi, W. Rekik and A. Oueslati, Synthesis, Structural characterization and complex impedance analysis of a novel organic-inorganic hybrid compound based on Mercury (II) chloride, *J. Mol. Struct.*, 2024, **1315**, 138881, DOI: 10.1016/j.molstruc.2024.138881.

31 S. Karmakar, S. Varma and D. Behera, Investigation of structural and electrical transport properties of nano-flower shaped NiCo2O4 supercapacitor electrode materials, *J. Alloys Compd.*, 2018, **757**, 49–59, DOI: 10.1016/j.jallcom.2018.05.056.

32 M. Singh, *et al.*, High Ionic Conduction and Polarity-Induced Piezo response in Layered Bimetallic Rb4Ag2BiBr9 Single Crystals, *J. Phys. Chem. C*, 2022, **126**(51), 21810–21824, DOI: 10.1021/acs.jpcc.2c06844.

33 S. Chkoundali, I. Garoui, W. Trigui and A. Oueslati, Crystal structure, Hirshfeld surface analysis, conduction mechanism and electrical modulus study of the new organic–inorganic compound [C8H10NO]2HgBr4, *RSC Adv.*, 2024, **14**(13), 8971–8980, DOI: 10.1039/d4ra00689e.

34 M. ben gzaiel, I. Garoui, F. N. Almutairi, I. Mbarek and O. Abderrazek, Lead-Free halide perovskites for optoelectronic application: Investigation of structural, optical, electric and dielectric behaviors, *Opt. Mater.*, 2024, **154**, 115664, DOI: 10.1016/j.optmat.2024.115664.

35 S.-P. Shen, *et al.*, Low-temperature fabrication of NASICON-type LATP with superior ionic conductivity, *Ceram. Int.*, 2022, **48**(24), 36961–36967, DOI: 10.1016/j.ceramint.2022.08.264.

36 B. K. Das, T. Das and D. Das, Structural and electrical properties of mechanically alloyed ZnO nanoceramic for NTC thermistor application, *J. Mater. Sci.: Mater. Electron.*, 2023, **34**(3), 230, DOI: 10.1007/s10854-022-09670-z.

37 C. Yuan, X. Liu, M. Liang, C. Zhou and H. Wang, Electrical properties of Sr–Bi–Mn–Fe–O thick-film NTC thermistors prepared by screen printing, *Sens. Actuators, A*, 2011, **167**(2), 291–296, DOI: 10.1016/j.sna.2011.02.047.

38 Z. P. Nenova and T. G. Nenov, Linearization Circuit of the Thermistor Connection, *IEEE Trans. Instrum. Meas.*, 2009, **58**(2), 441–449, DOI: 10.1109/tim.2008.2003320.

39 Y. Moualhi, H. Rahmouni and F. Bahri, Doublet doped titanate ferroelectric system for capacitors and NTC thermistor applications, *Sens. Actuators, A*, 2024, **377**, 115596, DOI: 10.1016/j.sna.2024.115596.

40 P. Umadevi, C. L. Nagendra and G. K. M. Thutupalli, Structural, electrical and infrared optical properties of vanadium pentoxide (V2O5) thick-film thermistors, *Sens. Actuators, A*, 1993, **39**(1), 59–69, DOI: 10.1016/0924-4247(93)80183-h.

41 S. Jagtap, S. Rane, S. Gosavi, U. Mulik and D. Amalnerkar, Infrared properties of 'lead free' thick film NTC thermo-resistive sensor based on the mixture of spinel material and RuO2, *Sens. Actuators, A*, 2013, **197**, 166–170, DOI: 10.1016/j.sna.2013.03.037.

42 D. Saha, A. Das Sharma, A. Sen and H. S. Maiti, Preparation of bixbyite phase (MnxFe1−x)2O3 for NTC thermistor applications, *Mater. Lett.*, 2002, **55**(6), 403–406, DOI: 10.1016/s0167-577x(02)00402-0.

43 Y. Q. Gao, *et al.*, Structural and electrical properties of Mn1.56Co0.96Ni0.48O4 NTC thermistor films, *Mater. Sci. Eng., B*, 2014, **185**, 74–78, DOI: 10.1016/j.mseb.2014.02.011.

44 R. Sagar, S. Madolappa, N. Sharanappa and R. L. Raibagkar, Synthesis, structure and electrical studies of praseodymium doped barium zirconium titanate, *Mater. Chem. Phys.*, 2013, **140**(1), 119–125, DOI: 10.1016/j.matchemphys.2013.03.009.

45 S. Sahoo, U. Dash, S. K. S. Parashar and S. M. Ali, Frequency and temperature dependent electrical characteristics of CaTiO3 nano-ceramic prepared by high-energy ball milling, *J. Adv. Ceram.*, 2013, **2**(3), 291–300, DOI: 10.1007/s40145-013-0075-8.

46 C. L. YUAN, X. Y. LIU, J. W. XU, X. W. ZHANG and C. R. ZHOU, Electrical properties of Sr x Ba1 − x Fe 0·6 Sn 0·4 O3 − ε NTC thermistors, *Bull. Mater. Sci.*, 2012, **35**(3), 425–431, DOI: 10.1007/s12034-012-0294-6.

47 J.-E. Kang, *et al.*, LaNiO3 conducting particle dispersed NiMn2O4 nanocomposite NTC thermistor thick films by aerosol deposition, *J. Alloys Compd.*, 2012, **534**, 70–73, DOI: 10.1016/j.jallcom.2012.04.038.

48 T. Nagai and M. Itoh, SiC thin-film thermistors, *IEEE Trans. Ind. Appl.*, 1990, **26**(6), 1139–1143, DOI: 10.1109/28.62400.

49 B. Zhang, Q. Zhao, A. Chang, H. Ye, S. Chen and Y. Wu, New negative temperature coefficient thermistor ceramics in Mn-doped CaCu3−xMnxTi4O12 (0≤x≤1) system, *Ceram. Int.*, 2014, **40**(7), 11221–11227, DOI: 10.1016/j.ceramint.2014.03.165.

50 R. N. Jadhav, S. N. Mathad and V. Puri, Studies on the properties of Ni0.6Cu0.4Mn2O4 NTC ceramic due to Fe doping, *Ceram. Int.*, 2012, **38**(6), 5181–5188, DOI: 10.1016/j.ceramint.2012.03.024.

51 S. Jagtap, S. Rane, U. Mulik and D. Amalnerkar, Thick film NTC thermistor for wide range of temperature sensing, *Microelectron. Int.*, 2007, **24**(2), 7–13, DOI: 10.1108/13565360710745539.

52 T. Rhimi, G. Leroy, B. Duponchel, K. Khirouni, S. Guermazi and M. Toumi, AC and DC conductivity study of LiH2PO4 compound using impedance spectroscopy, *Ionics*, 2017, **24**(5), 1305–1312, DOI: 10.1007/s11581-017-2306-4.

53 M. Krichen, M. Gargouri, K. Guidara and M. Megdiche, Phase transition and electrical investigation in lithium copper pyrophosphate compound Li2CuP2O7 using impedance spectroscopy, *Ionics*, 2017, **23**(12), 3309–3322, DOI: 10.1007/s11581-017-2161-3.

54 M. Javed, Y. Moualhi, N. Akbar, A. Masood, T. Alomayri and S. A. Muhammed Ali, Electrical dynamics and Havriliak-Negami dielectric relaxation behavior of FeNi2O4 electromagnetic spinel nickelate, *Ceram. Int.*, 2025, **51**(19), 28109–28121, DOI: 10.1016/j.ceramint.2025.04.025.

55 S. Aydi, M. M. Bouzayeni, I. Chaabane, N. A. Alghamdi, R. Barille and A. Oueslati, Enhanced Structural, Dielectric, Electrical, and Optical Properties of Ca2+/Sr2+ Doped LaNbO4 Ceramics, *Ceram. Int.*, 2025, **52**(2), 2314–2331, DOI: 10.1016/j.ceramint.2025.12.051.

56 W. H. Shah, *et al.*, Structural, dielectric relaxation, and electrical transport properties of Ca2V2O7 pyrovanadate: Complex impedance spectroscopy and DFT investigations, *Ceram. Int.*, 2025, **51**(25), 46294–46311, DOI: 10.1016/j.ceramint.2025.07.337.

57 K. S. Chikara, A. K. Bera, A. Kumar and S. M. Yusuf, Role of Crystal Structure on the Ionic Conduction and Electrical Properties of Germanate Compounds A2Cu3Ge4O12 (A = Na, K), *ACS Appl. Electron. Mater.*, 2023, **5**(5), 2704–2717, DOI: 10.1021/acsaelm.3c00176.

58 A. Rashid and M. Ikram, Dielectric behavior, Complex modulus, and conduction mechanism studies of Ni-doped La2SrFe2-xNixTiO9 triple perovskite for high-frequency electronic applications, *Mater. Sci. Eng., B*, 2025, **319**, 118332, DOI: 10.1016/j.mseb.2025.118332.

59 M. Mallek, I. Garoui, F. N. Almutairi, I. Chaabane, W. Rekik and A. Oueslati, Synthesis, structural characterization, Hirshfeld surface analysis, and electrical properties of a zinc (II)-based organic–inorganic hybrid compound, *J. Mater. Sci.: Mater. Electron.*, 2025, **36**(8), 458, DOI: 10.1007/s10854-025-14480-0.

60 F. Missaoui, *et al.*, Structural, dielectric and transport properties of NaxFe1/2Mn1/2O2 (x = 1 and 2/3), *RSC Adv.*, 2023, **13**(26), 17923–17934, DOI: 10.1039/d3ra02570e.

61 I. Ben Slima, K. Karoui, A. Mahmoud, F. Boschini and A. Ben Rhaiem, Structural, optical, electric and dielectric characterization of a NaCu0.2Fe0.3Mn0.5O2 compound, *RSC Adv.*, 2022, **12**(3), 1563–1570, DOI: 10.1039/d1ra08263a.